Clustering of floating tracer due to mesoscale vortex and submesoscale fields

Dmitry V. Stepanov[1], Eugene A. Ryzhov[1], Alexei A. Zagumennov[3], Pavel Berloff[2], Konstantin V. Koshel[1]

[1]V.I.Il'ichev Pacific Oceanological Institute of FEB RAS, 43, Baltiyskaya Street, Vladivostok, 690041, Russia
[2]Department of Mathematics, Imperial College London, London, SW7 2AZ, United Kingdom
[3]Institute of Automation and Control Processes FEB RAS, 5, Radio Street, Vladivostok, 690041, Russia

Key Points:

- Phenomenology of floating tracer clustering in the flow dominated by oceanic mesoscale vortices;
- Exponential clustering process is analyzed depending on the submesoscale model characteristics.
- It is argued that the 2D velocity field divergence is essential for studying tracer transport properties.

Corresponding author: Dmitry Stepanov, `step-nov@poi.dvo.ru`

Abstract

Floating tracer clustering is studied in oceanic flows that combine both a field of coherent mesoscale vortices simulated by a regional, comprehensive, eddy-resolving general circulation model and randomly modeled submesoscale velocity fields. Both fields have rotational and divergent velocity components, and depending on their relative contributions as well as on the local characteristics of the mesoscale vortices, we reported different clustering scenarios. We found that inclusion of the mesoscale vortices does not prevent clustering, but the rates and patterns of clustering become significantly modified. We also demonstrated that even when the surface velocity divergence is weak, it has to be taken into account to avoid significant errors in model predictions of the floating tracer patterns. Our approach combining dynamically constrained and random velocity fields, and the applied diagnostic methods, are proposed as standard tools for analyses and predictions of floating tracer distributions, both in observational data and general circulation models.

Plain language summary

The problem of dispersion and aggregation of various tracers in the ocean has recently attracted a lot of interest. These tracers can be natural ocean water characteristics such as temperature and salinity or various hazardous impurities such as plastic pollution and oil spills. A curious phenomenon of the tracer evolution is clustering, that is when the tracer is aggregated in isolated patches. Understanding and predicting tracer evolution in the ocean is one of the greatest challenges of today oceanography. Despite the fact that the ocean currents are largely two-dimensional, which means that the horizontal velocities significantly exceed the vertical one, the tracer evolution is nevertheless highly dependent on the vertical velocity. The drastic effect of the vertical velocity on the tracer clustering patterns is reported and analyzed. The importance of taking into account the vertical velocity when studying tracer evolution is highlighted.

1 Introduction

Mesoscale eddies are a ubiquitous component of the ocean circulation that significantly contributes to the material transport of oceanic properties and tracers, such as density, salinity, marine life and pollution. The corresponding background literature is immense and the involved theoretical aspects are comprehensively reviewed in (McWilliams, 2008; Samelson, 2013). For the purposes of this study, we note that coherent mesoscale vortices constitute substantial part of the total eddy field (Barbosa Aguiar, Peliz, & Carton, 2013; Chelton, Schlax, & Samelson, 2011; Chelton, Schlax, Samelson, & de Szoeke, 2007; Martínez-Moreno, Hogg, Kiss, Constantinou, & Morrison, 2019), contribute significantly to the material transport, and are remarkably long-lived and structurally organized, as opposed to more random and wave-like eddies around them.

Ocean circulation at the scales smaller than the mesoscale is dominated by the broad range of submesoscale processes, which have been intensively studied (Berta, Griffa, Özgökmen, & Poje, 2016; Berti, Santos, Lacorata, & Vulpiani, 2011; Haza, Özgökmen, & Hogan, 2016; McWilliams, 2016; Ohlmann, Romero, Pallàs-Sanz, & Perez-Brunius, 2019; Schroeder et al., 2012; Zhong & Bracco, 2013). Interactions between submesoscale and mesoscale motions are essential in the processes involved in formation and breakdown of coherent mesoscale vortices, but the progress in the theoretical understanding is hindered by overwhelming computational costs due to the spatial resolution requirements (Dauhajre, McWilliams, & Renault, 2019). An efficient way (though, with obvious limitations) to study these interactions is by employing kinematic models for submesoscale, whereas retaining dynamical modeling of mesoscale — this is the approach adopted in our study and applied to the tracer clustering phenomena.

Although, it is well-established that both in the ocean and atmosphere floating tracers tend to form spatially localised aggregations (Cozar et al., 2014; Law et al., 2010; Martinez, Maamaatuaiahutapu, & Taillandier, 2009; Maximenko, Hafner, & Niiler, 2012; McComb, 1990; Okubo, 1980; Väli, Zhurbas, Laanemets, & Lips, 2018), referred to as *clusters*, their exact definitions, as well as the existing measures of the degree of clustering, differ across various settings (Huntley, Lipphardt Jr., Jacobs, & Kirwan Jr., 2015; Jacobs et al., 2016). Dynamics of *floating* tracers is fundamentally different from the dynamics of *passive* tracers, because in the former case the tracer density on fluid particles additionally changes due to the experienced surface-velocity divergence, whereas in the latter case it is materially conserved and simply advected by the flow. In other words, the floating-tracer density is compressible and can not be fully described by concentrations of Lagrangian particles — this fundamental theoretical issue escaped attention of many previous studies that focused on the Lagrangian transport on the ocean surface (Cedarholm, Rypina, Macdonald, & Yoshida, 2019; Olascoaga et al., 2013; Prants, Budyansky, & Uleysky, 2018; Wang, Olascoaga, & Beron-Vera, 2015). Physical mechanisms leading to formation of clusters are also different and overall remain poorly understood, and our study deals with clustering due to divergence of the velocity (Law et al., 2010), which is present both in the mesoscale and submesoscale motions.

In this study we focus on the tracers *floating* on the ocean surface and directly experiencing only the 2D surface velocity component of the ocean circulation. We define clusters as small and transient areas that exponentially shrink in time and contain the tracer density that exponentially grows in time (Isichenko, 1992; Klyatskin & Koshel, 2000). This type of *exponential clustering* results from non-zero divergence of a 2D velocity field, such as the oceanic surface velocity affecting floating tracers. The asymptotic theory of clustering in random velocity fields (Klyatskin, 2015) states that the exponential clustering occurs necessarily, if the divergent component of the velocity completely dominates over the rotational component. When both components are comparable, a recent numerical modeling study of floating tracers in kinematic velocity fields suggests that the exponential clustering persists but its properties become altered (Koshel, Stepanov, Ryzhov, Berloff, & Klyatskin, 2019). The main restriction of the above study is in the use of purely kinematic multiscale velocities, whereas the main novelty of the present work is in the partial removal of this restriction by dynamically constraining the mesoscale component of the flow field.

This Letter aims at establishing phenomenology of possible clustering scenarios for floating tracers in the previously unstudied flows with dynamically modeled coherent mesoscale vortices (supplied by a comprehensive general circulation model) and kinematically modeled submesoscale flow component (represented as a random field).

2 Statement of the problem

In this section we describe how the models for the submesoscale and mesoscale velocity components were formulated, and how the tracer density fields were obtained.

A floating tracer is generally advected by a 2D flow with velocity $\mathbf{U}(\mathbf{R},t) = (u(\mathbf{r},t), v(\mathbf{r},t))\,|_{z=0}$ characterized by the divergence

$$\nabla_{\mathbf{R}}\mathbf{U}(\mathbf{R},t) = -\frac{\partial w(\mathbf{r},t)}{\partial z}\,|_{z=0}\ , \tag{1}$$

where $\mathbf{r} = (x,y,z)$ is the full position vector; $\mathbf{R} = (x,y)$ is the horizontal position vector; $\nabla_{\mathbf{R}}\mathbf{U}(\mathbf{R},t)$ is the horizontal divergence at the ocean surface ($z = 0$); and $w(\mathbf{r},t)$ is the vertical velocity component.

Since there is no vertical density flux of the floating tracer, the evolution of floating-tracer density $\rho(\mathbf{r},t)$ in the velocity field is governed by the material conservation equa-

tion:

$$\left(\frac{\partial}{\partial t} + \nabla_{\mathbf{R}}\mathbf{U}(\mathbf{R},t)\right)\rho(\mathbf{R},t) = 0\,, \qquad \rho(\mathbf{R},0) = \rho_0(\mathbf{R})\,, \tag{2}$$

and the total mass of the tracer is conserved: $M = \int d\mathbf{R}\rho(\mathbf{R},t) = const$. We treat the above equation and the velocity field in a nondimensional form, with the space, time and density scales denoted as L_0, t_0 and ρ^*, respectively, and chosen to be a typical mesoscale vortex size (i.e., of the order of the first baroclinic Rossby deformation radius), a typical turnover time, and the initial density (distributed over an area of the unity size); and the velocity scale follows from this as $U^* = L_0/t_0$. In dimensional units, the velocity scale is 2.0 m/s, whilst the characteristic regular velocity is of the order of magnitude less, i.e., about 0.2 m/s.

2.1 Mesoscale velocity model

The dynamically constrained combination of coherent mesoscale vortices and large-scale flow is referred to as the *regular component* of the velocity field. It is provided in terms of solution of an eddy-resolving (1/12-degree), regional, hydrostatic Boussinesq, sigma-coordinate, INMOM model (Diansky, Stepanov, Gusev, & Novotryasov, 2016; Stepanov, Diansky, & Novotryasov, 2014) configured for the Japan/East Sea (JES) region, plus the Sea of Okhotsk and adjacent parts of the Pacific Ocean. It is driven by the atmospheric forcing provided by the JRA55-do dataset covering the 1958-2017 period, and incorporating climatological boundary conditions on the open boundaries of the domain (Stepanov, Diansky, & Fomin, 2018). The simulated circulation of the JES is consistent with the existing observations (Diansky et al., 2016; Stepanov et al., 2014).

Following the approach of (Chelton, deSzoeke, Schlax, El Naggar, & Siwertz, 1998; Stepanov, 2017), we estimated the first baroclinic Rossby radius of deformation in the southeastern part of the Japan/East Sea to be in the range of $14 - 18$ km.

The simulated solution is averaged over one-month intervals (Fig. 1b), and one of its monthly averaged surface velocity snapshots (March 2000) in the south-western JES region is used for the follow-up analyses. To validate the simulated velocity field, we overlaid it with the corresponding monthly mean sea surface temperature (SST) field data provided by the AVHRR (Advanced Very-High-Resolution Radiometer) mounted on the satellites NOAA-12 and NOAA-15. This data was obtained pointwise, from 92 satellite images covering March 2000 (excluding the instances contaminated by clouds, which results in the absolute minimum of 8 images for a point). The simulated surface velocity and the observed SST have clearly similar patterns (e.g., well-pronounced separation of the warm and cold waters coincides with the flow pattern). Moreover, the modeled SST demonstrates similar patterns with the pronounced front delineating the cold northern water and the warm southern water. This correspondence ensures us that the modeled mesoscale velocity field reflects the real dynamical regimes in the JES system reliably well.

Since our main objective is to reveal clustering phenomena affected by coherent mesoscale vortices, we have chosen the sub-domain containing pronounced vortices and horizontally sheared flows (the grey square in Fig. 1 corresponds to the vorticity field (left panel) and the divergence field (right panel) in Fig. 2). Specified areas of interest are designated (fig. 2) as C_1 (for a cyclonic eddy), A_2 (for two weak anticyclonic eddies) and A_1 (for the pair of cyclone and anticyclone). These regions serve as typical configurations of various vortex-dominant regimes with distinctive Lagrangian particle spreading patterns.

We emphasise that, as a starting point, we are interested in clustering phenomena that proliferate much faster than the characteristic time scale of the underlying mesoscale (regular) velocity field. This allows us to consider the stationary mesoscale velocity field by taking its monthly average.

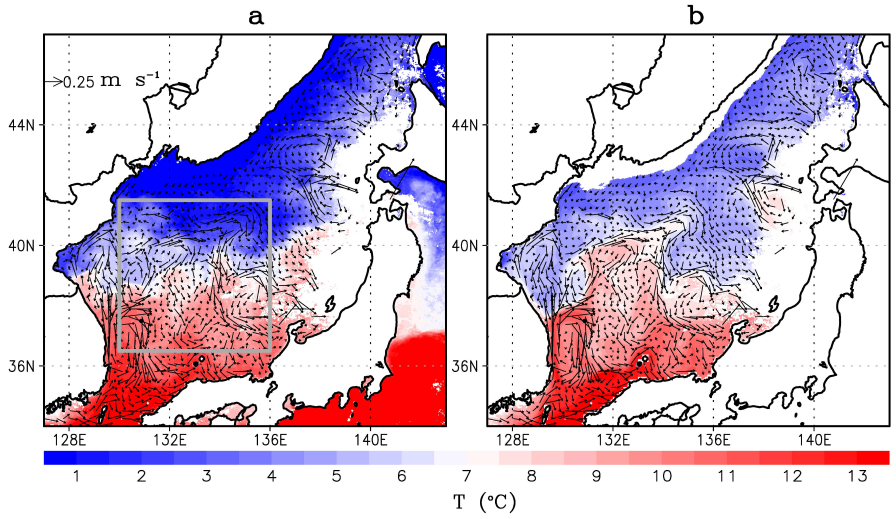

Figure 1: A monthly mean (March 2000) sea surface regular velocity field from the numerical simulation of the Japan/East Sea circulation (the vector fields in both panels); the corresponding monthly mean sea surface temperature (colour shading, in degrees of Celsius) from satellite observations (a) and from numerical simulation (b). The general circulation patterns are reliably captured by the simulation, so that the warm and cold regions of the JES are separated by the intense meandering jet with the adjacent mesoscale vortices. The grey square indicates the subdomain of interest, robustly populated by many mesoscale coherent structures.

Note, that the characteristic divergence for the regular velocity is $\approx 10^{-6}\ s^{-1}$ (see the top-right panel in fig. 2), whilst the random velocity divergence is orders of magnitude larger $\approx 10^{-2}\ s^{-1}$.

2.2 Submesoscale velocity model

The 2D *divergent* velocity field $\mathbf{U}$ is chosen to be random, normally distributed, spatially homogeneous, isotropic, and stationary; it is also a linear combination of the mean (given by the regular stationary mesoscale field, which is the mean state of the modelled March 2000 interval, as introduced in section 2.1), divergent and rotational components:

$$\mathbf{U}(\mathbf{R},t) = \underbrace{\langle \mathbf{U}(\mathbf{R},t) \rangle}_{\textbf{mesoscale}} + \underbrace{\gamma \mathbf{U}^p(\mathbf{R},t) + (1-\gamma)\mathbf{U}^s(\mathbf{R},t)}_{\textbf{submesoscale}}, \tag{3}$$

where superscript p indicates the divergent (irrotational) component, superscript s indicates the rotational (nondivergent) component, and parameter $0 \le \gamma \le 1$ sets their relative contributions. The mesoscale part corresponds to the monthly averaged regular velocity field, and the submesoscale is represented by the random field.

Our next goal is to formulate a model for random, spatially correlated, and temporally uncorrelated (i.e., δ-correlated), kinematic velocity field; for this purpose we define (Klyatskin, 1994, 2015) the correlation tensor:

$$B^j_{\alpha\beta}(\mathbf{R}',\eta) = \langle U^j_\alpha(\mathbf{R},t) U^j_\beta(\mathbf{R}+\mathbf{R}',t+\eta)\rangle = \int d\mathbf{k} E^j_{\alpha\beta}(\mathbf{k},\eta) e^{i\mathbf{k}\mathbf{R}'}\,, \tag{4}$$

where indices α and β stand for x and y and indicate different components of the tensor; and index j stands for p and s, and indicates different tensors; and the following spec-

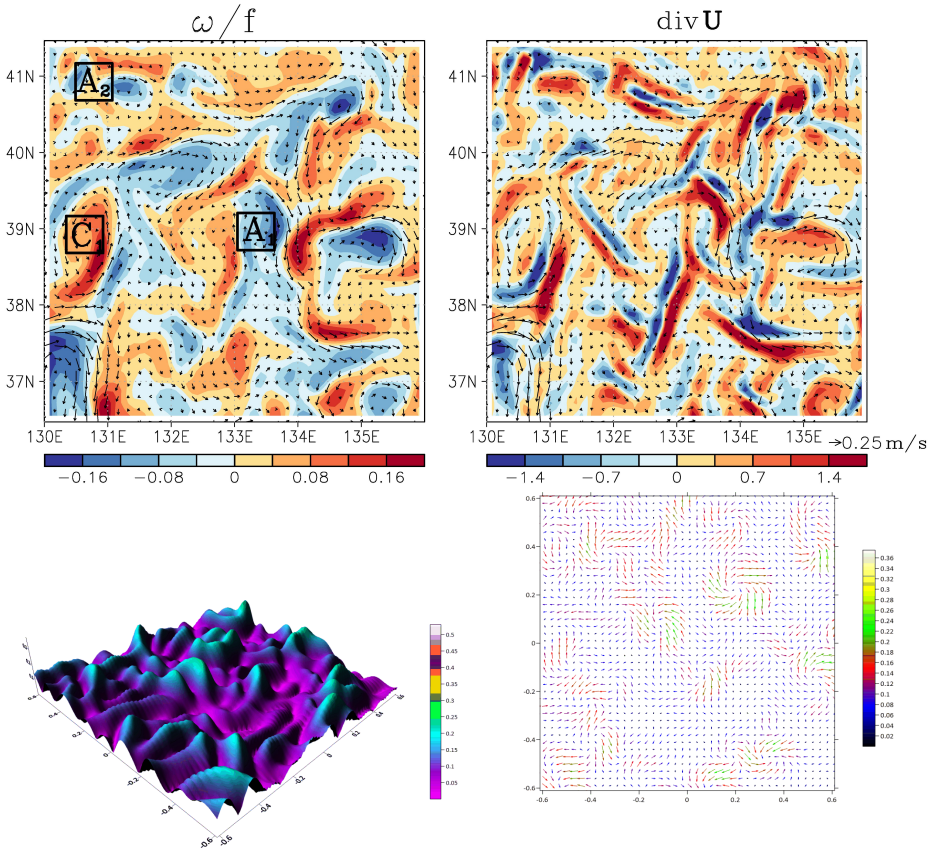

Figure 2: Top row: stationary fields of the regular (mesoscale) stationary velocity fields. Left panel – vertical component of the relative vorticity vector normalized by the local Coriolis parameter; right panel – divergence (units are $10^{-6}s^{-1}$). The squares labelled as A_1, A_2 and C_1 denote the tracer deployment regions. Bottom row: instantaneous snapshots of a single realisation of the random velocity field in a subdomain enlarged for visibility for $\gamma = 0.5$. Left panel: a snapshot of random flow velocity absolute value; right panel: a snapshot of the random velocity field (color-coded).

tral densities are assumed:

$$E^p_{\alpha\beta}(\mathbf{k},\eta) = E^p(k,\eta)\frac{k_\alpha k_\beta}{k^2}\,, \qquad E^s_{\alpha\beta}(\mathbf{k},\eta) = E^s(k,\eta)\left(\delta_{\alpha\beta} - \frac{k_\alpha k_\beta}{k^2}\right). \tag{5}$$

The correlation tensor is nonzero only for the zero time lag η:

$$B^j_{\alpha\beta}(\mathbf{0},0) = \langle U^j_\alpha(\mathbf{R},t)U^j_\beta(\mathbf{R},t)\rangle = \frac{1}{2}\left(\sigma^j_{\mathbf{U}}\right)^2\delta_{\alpha\beta}, \tag{6}$$

where $\left(\sigma^j_{\mathbf{U}}\right)^2 = B^j_{\alpha\alpha}(\mathbf{0},0) = \int d\mathbf{k}E^j(k,0)$. In our case we choose $E^s = E^p = E$, and the amplitude of the spectral density is taken in the form

$$E(k,0;l) = \frac{1}{2\pi}\frac{l^4}{4}k^2\exp\left\{-\frac{1}{2}k^2l^2\right\}, \tag{7}$$

where l is the spatial correlation radius (a parameter of the random velocity field); the random phase functions used for the random velocity field generation depend explicitly on time (Klyatskin & Koshel, 2017). In numerical simulations, we use $\sigma^p_{\mathbf{U}} = \sigma^p_{\mathbf{U}} \sim 0.1$, which results in the typical velocity of 0.2 m/s (i.e. the same as for the regular velocity). The nondimensional correlation radius is 0.08 and in the dimension units is 2.0 km. The nondimensional integration time step is taken 0.01, which in dimensional units is 120 s.

2.3 Numerical implementation and methodology

To simulate the random submesoscale velocity field, we use spectral representation and uniform 2048×2048 grid. Details of the numerical implementations of the random velocity field can be found in (Klyatskin & Koshel, 2017). Since the random field is not differentiable in time, we solve the Lagrangian equivalent of (2),

$$\begin{aligned}
&\frac{d\mathbf{R}}{dt} = \mathbf{U}\left(\mathbf{R},t\right),\ \mathbf{R}\left(0\right) = \xi,\\
&\frac{d\rho}{dt} = -\nabla_{\mathbf{R}}\mathbf{U}(\mathbf{R},t)\rho\left(t\right),\ \rho\left(0\right) = \rho_0\left(\xi\right),
\end{aligned} \tag{8}$$

applied to ensembles of Lagrangian particles advected by the total velocity field and solved numerically by the method of characteristics (Klyatskin, 1994, 2015; Koshel & Alexandrova, 1999), where ξ is the initial position of each particle. Equations (8) are time-stepped using the standard Euler-Itô scheme (Kloeden & Platen, 1992; Klyatskin & Koshel, 2017; Koshel & Alexandrova, 1999), and the Eulerian density field can be obtained by the spatial interpolation, if needed. The regular velocity component is taken to be piecewise-constant over the same grid as the one used for the random component.

To analyze the clustering phenomena we employ the statistical topography methodology (Isichenko, 1992). One of the characteristics used in statistical topography is the *clustering area*, which is defined as the total combined area of the regions where the tracer density exceeds a certain threshold:

$$\langle S(t;\bar\rho)\rangle = \int d\mathbf{R}\ \langle\theta(\rho(\mathbf{R},t)-\bar\rho)\rangle = \int d\mathbf{R}\int\limits_{\bar\rho}^{\infty} d\rho'\,P(\mathbf{R},t;\rho')\,, \tag{9}$$

where $\theta\left(\cdot\right)$ is the Heaviside (step) function; and $P(\mathbf{R},t;\rho)$ is the probability density function (PDF) of the tracer density distribution. The other useful characteristics is the *clustering mass*, which is the amount of tracer aggregated within the clustering area:

$$\langle M(t;\bar\rho)\rangle = \int d\mathbf{R}\,\rho(\mathbf{R},t)\,\langle\theta(\rho(\mathbf{R},t)-\bar\rho)\rangle = \int d\mathbf{R}\int\limits_{\bar\rho}^{\infty} d\rho'\,\rho' P(\mathbf{R},t;\rho')\,. \tag{10}$$

In the exponential clustering regime for the floating tracer, the clustering area tends to zero, and the clustering mass tends to the unity (i.e., the clusters accumulate all the available tracer) in the asymptotic limit (Klyatskin, 2015; Klyatskin & Koshel, 2017). The exact analytical estimates for the clustering area and mass are derived in (Klyatskin, 2015) for the purely divergent velocity case:

$$\langle S(t;\bar{\rho})\rangle \sim exp(-\frac{1}{4}\tau)/\sqrt{\tau} = exp(-\frac{1}{4}D_p t)/\sqrt{D_p t}, \qquad \langle M(t;\bar{\rho})\rangle \sim 1 - \langle S(t;\bar{\rho})\rangle \ , \tag{11}$$

where $D_p = (\gamma^2\sigma_U^2/l^2)t_0$ is the effective diffusivity of the divergent velocity component. Most of our numerical simulations were carried out with $\sigma_U = 0.1$ and $l = 0.08$; for this set of parameters, we use notation D_0 instead of D_p.

We distribute 3 square-shaped tracer patches in the subdomain of interest (top-left panel in Fig. 2); each tracer patch contains 36×10^6 Lagrangian floating particles uniformly distributed within the squares. The number of particles deployed has been tested to be adequate in capturing the clustering phenomena. If the number of tracers is either doubled or halved, the clustering characteristic tendencies remain almost unchanged. Moreover, if we consider only the purely random velocity field (so $\gamma = 1$ and without the mean regular part), the numerical calculations follow very closely the asymptotic estimate (11) derived for this test case specifically. Thus, we are confident that the number of particles deployed is sufficient to establish the clustering properties accurately.

Four experiments have been devised to explore relative influence of the random velocity component on the resulting tracer density distribution. All the experiments employ the same regular velocity component, whilst the influence of the random velocity field varies such that

1. EXP1 employs only the regular velocity field and forms the reference solution to evaluate the effect of the submesoscale further;
2. EXP2 — plus the purely rotational random velocity field ($\gamma = 0$);
3. EXP3 — plus the purely divergent random velocity field ($\gamma = 1$);
4. EXP4 — plus the mixed random velocity field ($\gamma = 0.5$).

3 Clustering scenarios

In this section we describe results of the floating tracer clustering in the benchmark solutions.

3.1 Effect of submesoscales

The reference case EXP1 (i.e., with the random submesoscale component switched off) illustrates typical tracer patterns in the deployment regions (Fig. 3a). Stationary vortices retain the tracer; in the regions with no closed streamlines, the tracer is intensely stirred and spread out. Large values of tracer density (red colour) are rare and correspond to stationary sinks in the regular velocity field.

Now, we turn our attention to the benchmark solutions (EXP2, EXP3, and EXP4) featuring different submesoscale flow components. The purely rotational EXP2 solution (Fig. 3b) is characterized by smearing of the tracer patches due to enhanced tracer dispersion. A similar effect has been observed in the model of an isolated ellipsoidal vortex subject to random velocity perturbations (Koshel, Ryzhov, & Zhmur, 2013). Overall tracer patterns and density values are similar to EXP1 (Fig. 3a), but the boundaries of the tracer patches are more filamented due to the random fluctuations.

When the random velocity field is purely divergent (EXP3; $\gamma = 1$; Fig. 3c), the tracer evolution is characterized by the appearance of the exponential clustering, i.e. almost all of the tracer tends to congregate in clusters of anomalous density. The cluster-

ing pattern is developed and remains persistent in time (right panel of Fig. 3c). On the other hand, the overall large-scale pattern of the mesoscale-size tracer features, which is clearly seen in EXP2-4, is now qualitatively eroded. Remarkably, the exponential clustering develops within the mesoscale jets (intense unidirectional flows separating regions with distinct dynamical regimes) and vortices, uniformly from vortex periphery to core.

A similar small-scale pattern with pronounced graining is observed when the rotational and divergent submesoscale flow components are equally strong (EXP4; $\gamma = 0.5$), the tracer evolution is also characterized by the appearance of the exponential clustering (Fig. 3d) with its highly anomalous values of the tracer density (red colour). The large-scale tracer distribution pattern remains fairly similar to EXP1 and EXP2, but the small-scale pattern of the density becomes grainy and characterized by the large and growing density (a typical behaviour for the purely divergent case EXP3) — this is the manifestation of the exponential clustering.

Since our interest is mostly in the clustering process subject to coherent mesoscale vortices, we choose a typical situation — the cyclone over C_1 release location — and analyze the corresponding tracer evolution in detail (Fig. 4). In EXP1 the tracer is expelled towards periphery of the cyclone; in EXP2 it is additionally smeared across the mesoscale shear, and the boundary of the tracer patch is significantly more distorted; in EXP3 the exponential clustering is most pronounced with most of the tracer being aggregated in clusters (high anomalous density values coloured with red in Figs. 3 – 4); in EXP4 despite the strong influence of the rotational component, the exponential clustering still persists (there are many anomalous values in red, but not as many as in the purely divergent case EXP3). Qualitative differences between clustering dynamics of EXP3 and EXP4 are quantified in the next section.

It is worth noticing that clusters tend to aggregate differently in cyclones (tendency towards the periphery) and anticyclones (tendency towards the centre). For example, the tendency is clearly seen for initial deployment region A_1: the clusters cover the anticyclone's centre more densely.

For a partial interpretation of the modeling results, we resort to the existing theory of clustering in random velocity fields containing uniform-shear flow component (Klyatskin, 2015), which predicts the following time dependence of the single-particle dispersion:

$$\sigma_{xx}^2 = 2D_0 t(1 + \alpha t + \frac{1}{3}\alpha^2 t^2)\,, \qquad \sigma_{yy}^2 = 2D_0 t\,, \tag{12}$$

where α is the shear parameter. According to this estimate, a tracer patch should be smeared in time, more so along the shear direction (see this in Fig. 3b); moreover, in the case of purely rotational velocity field (i.e., no exponential clustering), the other estimate for the dispersion of the density gradient p is valid (Klyatskin, 2015):

$$\left\langle p^2\,(t)\right\rangle \sim \exp\left\{\left(\frac{3}{2}\alpha^2 D_s\right)^{1/3} t\right\}\,, \tag{13}$$

where D_s is the dispersion due to the purely rotational random velocity field. This estimate is obtained in the limit $D_s \ll \alpha$, when $\alpha \neq 0$, and its interpretation is the following: regardless of how small D_s is, it still contributes towards increasing the gradient dispersion, that is, it makes the tracer patch boundary more serrated (similar tendencies are seen in Fig. 3b), opposite to the (elongating) effect of uniform shear on the tracer patch. Although, the above estimate is valid for uniform shear, we expect it to be true for more complicated shears, and this expectation is consistent with the simulations discussed in this section.

To quantify clustering properties in the above-discussed scenarios, one can make use of statistical topography diagnostics, such as the clustering area and mass (Isichenko, 1992). In EXP4 the rate of exponential clustering (Fig. 5) is qualitatively similar (how-

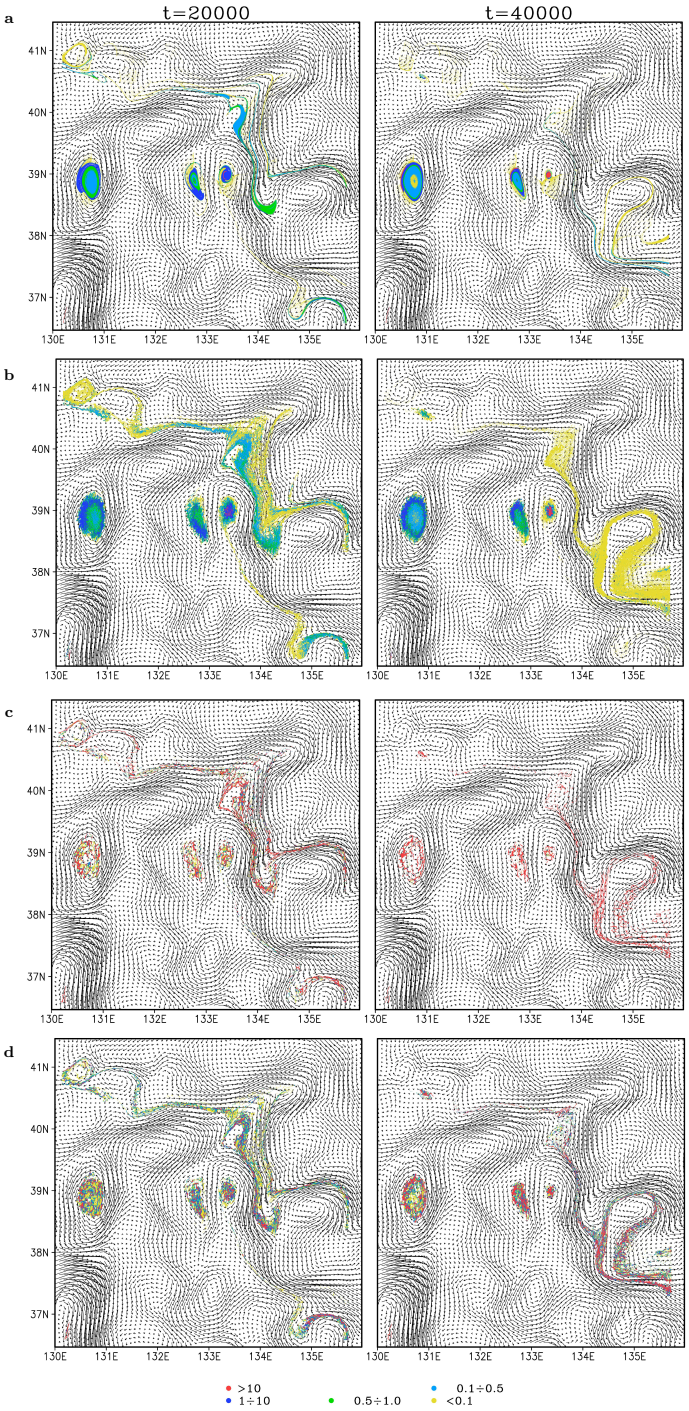

Figure 3: Tracer densities corresponding to (a) EXP1 – regular velocity component, no random velocity, (b) EXP2 – regular plus purely rotational random velocity component, (c) EXP3 – regular plus purely divergent random velocity component, (d) EXP4 – regular plus equal contributions ($\gamma = 0.5$) from the rotational and divergent random velocity components). Colour-coded is the dimensionless tracer density. Red values correspond to anomalous values, which indicate the exponential clustering. Anomalous values are dominant in the purely divergent case (c) and less so (however anomalous values are still rife) in the mixed case (d); The tracer advection patterns mostly remain the same since the regular component is stationary: the C_1-tracer remains bounded to the original deployment site; the A_1-tracer is redistributed within the cyclone-anticyclone pair; the A_2-tracer is advected southeastward.

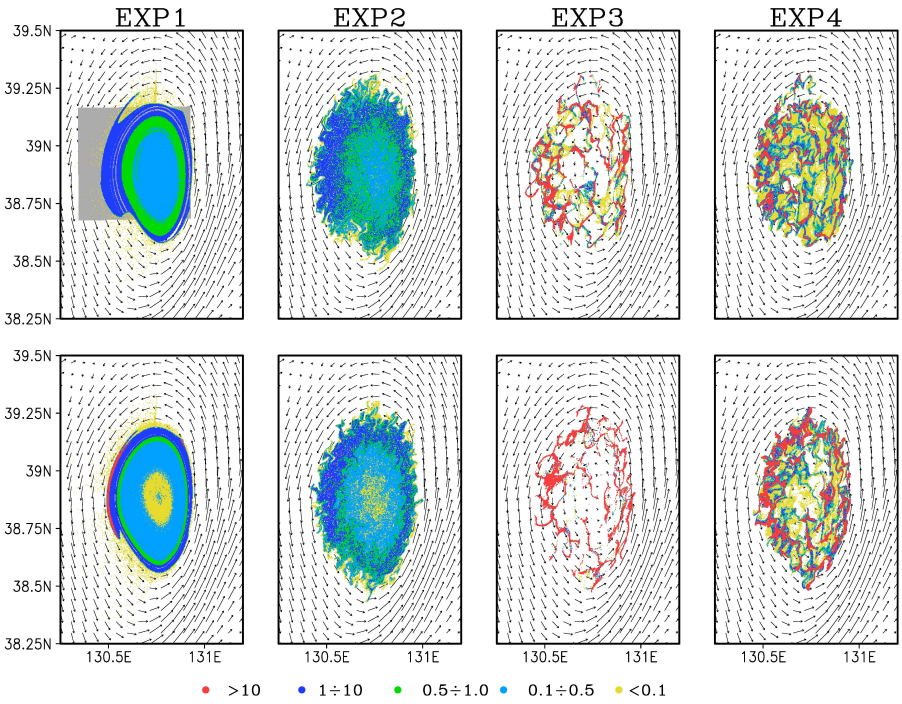

Figure 4: Tracer density for the benchmark experiments. The enlarged region corresponding to the C_1 tracer release location. Top and bottom rows correspond to consequent dimensionless time instances $t = 20000$ and 40000, respectively. The rest is as in Fig. 2.

ever, noticeably weaker) to the theoretical prediction for the purely divergent case EXP3 (Klyatskin, 2015; Klyatskin & Koshel, 2017; Koshel et al., 2019). Despite the general tendency towards the exponential clustering, the clustering process is significantly affected by the specifics of the regular velocity, as illustrated by different evolution curves for different locations of the initial tracer deployment (Fig. 5). Formation of clusters can be inhibited by intense shear in jet-like flows, as can be seen in Fig. 5 for the A_2 case.

Changing the random velocity field parameters σ_U and l is similar to changing the diffusivity. The clustering proxy curves calculated for different sets of the parameters (purple curve ($\sigma_U = 0.2, l = 0.04$) and thin black curves ($\sigma_U = 0.1, l = 0.16$) in fig. 5 and other combinations (not shown for brevity)) produce similar shapes of the curves. If D_p is decreased, the clustering slows down for larger values of clustering mass (Jacobs et al., 2016); if D_p is increased, the rate of clustering in the large-time limit (slow regime) decreases. Overall, the effective diffusivity cannot stop or initiate clustering, and only modifies it.

In the numerical experiments, we use a two-order-of-magnitude excess of the initial density value as a clustering threshold. The threshold is sufficient to categorize clustering, since the statistical topography characteristics change little when the threshold is further increased (we have checked three orders of magnitude). More importantly, the general exponential tendency (the black thick lines in Fig. 5) against which the numerical calculations are compared is clearly evident from the shapes of the lines for the purely divergent case EXP3, whilst the mixed velocity case EXP4 produces distorted curves.

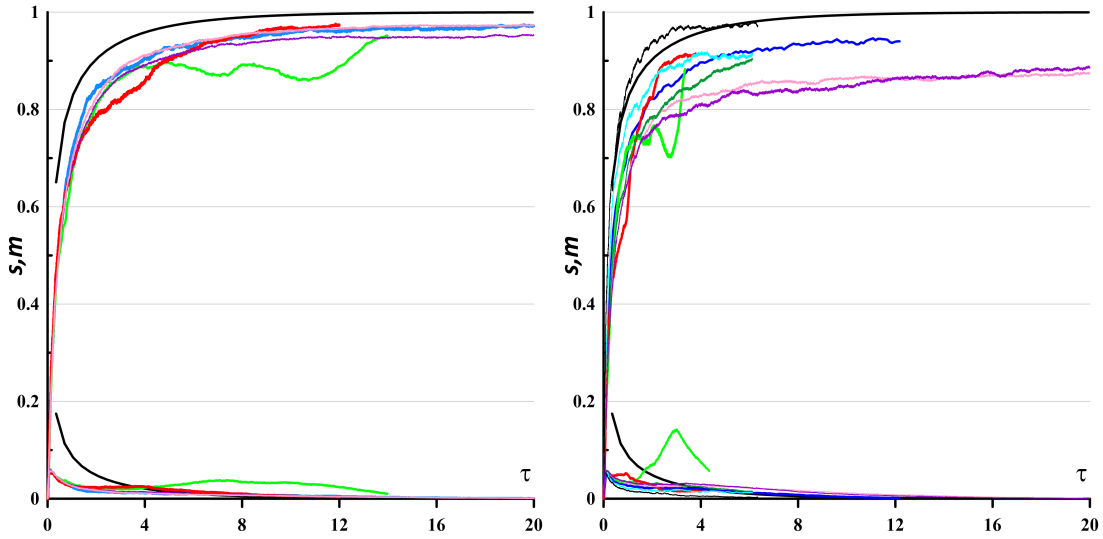

Figure 5: Time series of (top curves) clustering mass and (bottom curves) clustering area for EXP3 (left panel) and EXP4 (right panel) for the following tracer deployment locations: C_1 — blue lines, A_1 — red lines, and A_2 -– green lines ($\sigma_U = 0.1, l = 0.08$). The black curves show theoretical estimates (11) for the purely divergent case (EXP3). Additional two curves correspond to different sets of the parameters (σ_U, l) through eq. (11) and the tracer deployment location C_1: purple – $D_p = 16D_0$ ($\sigma_U = 0.2, l = 0.04$); thin black – $D_p = \frac{1}{4}D_0$ ($\sigma_U = 0.1, l = 0.16$). For most of the cases, the exponential nature of clustering is clearly evident.

4 Conclusions

This study was motivated by the well-established phenomenon of clustering, that is, the development of spatially localised aggregations, here, of floating tracers (e.g., marine plastic and other pollution, marine biomass) on the ocean surface. The underlying theory for this phenomenon remains largely undeveloped, except for simple kinematic, random velocity flows, which are our starting point. The main novelty of the present work is in considering effects manifested for the floating tracers and not for the passive ones. The other novelty is in terms of considering the phenomenology of clustering in the velocity field containing both random and regular (i.e., dynamically constrained) components. The latter component comes from a dynamical, realistic, general circulation model of the Japan/East Sea region and features mesoscale vortices. The former one aims at representing submesoscale motions unresolved by the dynamical model and is simulated by a random kinematic model.

Four experiments with gradually increased influence of the divergent component of the flow were devised to assess its relative influence on the clustering phenomena. Three regions of interest were selected, as representing typical footprints of the mesoscale eddies: an isolated cyclonic eddy; two anticyclonic eddies; a pair of cyclonic-anticyclonic eddies. We studied tracer clustering scenarios and patterns induced by these regular flows in combination with random velocity fields representing submesoscale motions. An important finding is that regions of intense shears, such as mesoscale vortices and jets, still support complete clustering scenarios, however, with significantly reduced rates, and even more so in anticyclones. We hypothesize that such behaviors occur in the real ocean, and this motivates relevant observational studies to be carried out, especially, in the light of growing concerns about the plastic and other environmental pollution and the need to understand and mitigate these processes.

A compelling feature of the presented clustering behaviour is the widespread distribution of intermittent patterns of floating-tracer clusters within such regions of intense shears, as vortices and jets. This suggests that real mesoscale eddies in the ocean should also contain similar patterns; although, the relevant observations are either scarce or with inadequate spatial resolution, we have reported an interesting case of such evidence. An example of mesoscale vortex footprint, extracted from the observed sea surface temperature field (Fig. 6) in the region of interest and at the time of interest, demonstrates a large number of cluster-like patterns close to the resolution limit of $\approx 1\ km$. Although, we may question whether these features are just resolution errors, their general inhomogeneous distribution suggests the dynamical origins and influences of submesoscale motions. Similar cluster patterns are seen in the model solution (Fig. 4), where populations of the clusters tend to occupy the periphery of the vortex. A serious challenge for further comparison between the model solution and observations are weak SST gradients, which make it difficult to disentangle specific contributions of the rotational and divergent velocity components that are shown to be essential for the rate and intensity of the clustering process. Another issue worth exploring is the influence of non-stationarity of the mesoscale field, which can lead to intense filamentation process thus altering the tracer evolution significantly. These avenues seem extremely promising in getting more insight in the complex multi-scale transport phenomena at the ocean surface.

Acknowledgments

This study was partially supported by the POI FEB RAS Program "Mathematical simulation and analysis of dynamical processes in the ocean" ($AAAA-A117030110034-7$) and by the Russian Foundation for Basic Research projects $19-55-10001$, $20-05-00083$. EAR and PB were supported by the NERC grant $NE/R011567/1$ and by the Royal Society Exchange Grant $IEC/R2/181033$. The contribution of KVK in obtaining the analytical estimates was supported by the Russian Scientific Foundation project $19-17-00006$. PB also gratefully acknowledges support from the NERC grant $NE/T002220/1$

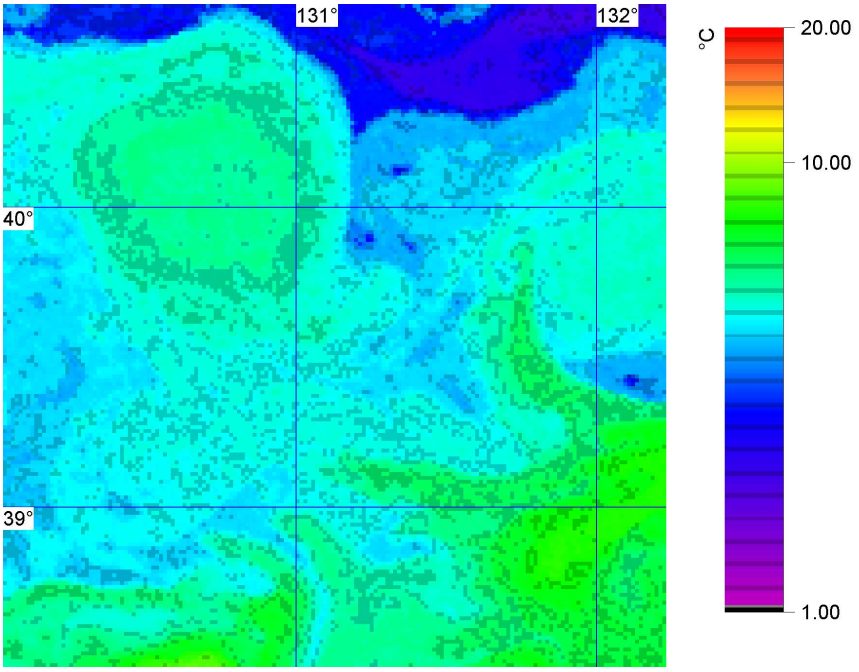

Figure 6: Temperature snapshot in the region of interest obtained from satellite observations (March 14, 2000) and showing pronounced mesoscale vortex in the upper-left section. Numerous small-scale anomalies, clearly seen within the eddy and around it, can be due to the clustering process induced by submesoscale motions.

and the Leverhulme grant *RPG* − 2019 − 024. The numerical simulation outputs were obtained using the Shared Resource Center "Far Eastern Computing Resource" IACP FEB RAS (`https://www.cc.dvo.ru`). Data are available `https://www.researchgate.net/publication/336133063_dataset_for_Geophysical_Research_Letters`.

References

Barbosa Aguiar, A. C., Peliz, A., & Carton, X. (2013). A census of meddies in a long-term high-resolution simulation. *Prog. Oceanogr.*, *116*, 80–94. doi: 10.1016/j.pocean.2013.06.016

Berta, M., Griffa, A., Özgökmen, T. M., & Poje, A. C. (2016). Submesoscale evolution of surface drifter triads in the gulf of mexico. *Geophys. Res. Lett.*, *43*(22), 11,751–11,759. doi: 10.1002/2016GL070357

Berti, S., Santos, F. A. D., Lacorata, G., & Vulpiani, A. (2011). Lagrangian drifter dispersion in the southwestern atlantic ocean. *J. Phys. Oceanogr.*, *41*(9), 1659–1672. doi: 10.1175/2011JPO4541.1

Cedarholm, E. R., Rypina, I. I., Macdonald, A. M., & Yoshida, S. (2019). Investigating subsurface pathways of fukushima cesium in the northwest pacific. *Geophys. Res. Lett.*, *46*(12), 6821-6829. doi: 10.1029/2019GL082500

Chelton, D. B., deSzoeke, R. A., Schlax, M. G., El Naggar, K., & Siwertz, N. (1998). Geographical variability of the first baroclinic rossby radius of deformation. *Journal of Physical Oceanography*, *28*(3), 433-460. doi: 10.1175/1520-0485(1998)028⟨0433:GVOTFB⟩2.0.CO;2

Chelton, D. B., Schlax, M. G., & Samelson, R. M. (2011). Global observations of nonlinear mesoscale eddies. *Prog. Oceanogr.*, *91*(2), 167–216.

Chelton, D. B., Schlax, M. G., Samelson, R. M., & de Szoeke, R. A. (2007). Global

observations of large oceanic eddies. *Geophys. Res. Lett.*, *34*, L15606.

Cozar, A., Echevarria, F., Gonzalez-Gordillo, J. I., Irigoien, X., Ubeda, B., Hernandez-Leon, S., ... Duarte, C. M. (2014). Plastic debris in the open ocean. *Proceedings of the National Academy of Sciences*, *111*, 10239-10244. doi: 10.1073/pnas.1314705111

Dauhajre, D. P., McWilliams, J. C., & Renault, L. (2019). Nearshore lagrangian connectivity: Submesoscale influence and resolution sensitivity. *J. Geophys. Res.: Oceans*, *124*(7), 5180–5204. doi: 10.1029/2019JC014943

Diansky, N. A., Stepanov, D. V., Gusev, A. V., & Novotryasov, V. V. (2016). Role of wind and thermal forcing in the formation of the water circulation variability in the Japan/East Sea Central Basin in 1958–2006. *Izvestiya, Atmospheric and Oceanic Physics*, *52*, 207–216. doi: 10.1134/S0001433816010023

Haza, A. C., Özgökmen, T. M., & Hogan, P. (2016). Impact of submesoscales on surface material distribution in a gulf of mexico mesoscale eddy. *Ocean Modelling*, *107*, 28 - 47. doi: https://doi.org/10.1016/j.ocemod.2016.10.002

Huntley, H. S., Lipphardt Jr., B. L., Jacobs, G., & Kirwan Jr., A. D. (2015). Clusters, deformation, and dilation: Diagnostics for material accumulation regions. *J. Geophys. Res.: Oceans*, *120*(10), 6622-6636. doi: 10.1002/2015JC011036

Isichenko, M. B. (1992). Percolation, statistical topography, and transport in random media. *Rev. Mod. Phys.*, *64*, 961–1043. doi: 10.1103/RevModPhys.64.961

Jacobs, G. A., Huntley, H. S., Kirwan Jr., A. D., Lipphardt Jr., B. L., Campbell, T., Smith, T., ... Bartels, B. (2016). Ocean processes underlying surface clustering. *Journal of Geophysical Research: Oceans*, *121*(1), 180-197. doi: 10.1002/2015JC011140

Kloeden, P., & Platen, E. (1992). *Numerical solution of stochastic differential equations*. Springer, Berlin.

Klyatskin, V. I. (1994). Statistical description of the diffusion of a passive tracer in a random velocity field. *Physics-Uspekhi*, *37*, 501–513.

Klyatskin, V. I. (2015). *Stochastic equations: Theory and applications in acoustics, hydrodynamics, magnetohydrodynamics, and radiophysics* (Vols. 1,2). Springer.

Klyatskin, V. I., & Koshel, K. (2017). Impact of diffusion on surface clustering in random hydrodynamic flows. *Phys. Rev. E*, *95*, 013109. doi: 10.1103/PhysRevE.95.013109

Klyatskin, V. I., & Koshel, K. V. (2000). The simplest example of the development of a cluster-structured passive tracer field in random flows. *Physics-Uspekhi*, *170*, 771–778.

Koshel, K. V., & Alexandrova, O. V. (1999). Some results of a numerical modeling of the diffusion of passive tracers in a random field of velocities. *Izv. Atmos. Ocean. Phys.*, *35*, 578–588.

Koshel, K. V., Ryzhov, E. A., & Zhmur, V. V. (2013). Diffusion-affected passive scalar transport in an ellipsoidal vortex in a shear flow. *Nonlin. Processes Geophys.*, *20*, 437–444. doi: 10.5194/npg-20-437-2013

Koshel, K. V., Stepanov, D. V., Ryzhov, E. A., Berloff, P. S., & Klyatskin, V. I. (2019). Clustering of floating tracers in weakly divergent velocity fields. *ArXiv*, 1906.10291.

Law, K. L., Moret-Ferguson, S., Maximenko, N. A., Proskurowski, G., Peacock, E. E., Hafner, J., & Reddy, C. M. (2010). Plastic accumulation in the north atlantic subtropical gyre. *Science*, *329*, 1185-1188. doi: 10.1126/science.1192321

Martinez, E., Maamaatuaiahutapu, K., & Taillandier, V. (2009). Floating marine debris surface drift: Convergence and accumulation toward the south pacific subtropical gyre. *Marine Pollution Bulletin*, *58*, 1347 – 1355.

Martínez-Moreno, J., Hogg, A. M., Kiss, A. E., Constantinou, N. C., & Morrison,

A. K. (2019). Kinetic energy of eddy-like features from sea surface altimetry. *Journal of Advances in Modeling Earth Systems*, *11*(10), 3090-3105. doi: 10.1029/2019MS001769

Maximenko, N., Hafner, J., & Niiler, P. (2012). Pathways of marine debris derived from trajectories of lagrangian drifters. *Marine Pollution Bulletin*, *65*(1-3), 51–62. doi: 10.1016/j.marpolbul.2011.04.016

McComb, W. D. (1990). *The physics of fluid turbulence* (Vol. 25). Oxford: Clarendon Press.

McWilliams, J. C. (2008). The nature and consequences of oceanic eddies. In *Ocean modeling in an eddying regime* (p. 5-15). American Geophysical Union (AGU). doi: 10.1029/177GM03

McWilliams, J. C. (2016). Submesoscale currents in the ocean. *Proc. R. Soc. A*, *472*, 20160117. doi: 10.1098/rspa.2016.0117

Ohlmann, J. C., Romero, L., Pallàs-Sanz, E., & Perez-Brunius, P. (2019). Anisotropy in coastal ocean relative dispersion observations. *Geophys. Res. Lett.*, *46*(2), 879–888. doi: 10.1029/2018GL081186

Okubo, A. (1980). *Diffusion and ecological problems: Mathematical models* (Vol. 10). Berlin: Springer-Verlag.

Olascoaga, M. J., Beron-Vera, F. J., Haller, G., Trinanes, J., Iskandarani, M., Coelho, E. F., ... Valle-Levinson, A. (2013). Drifter motion in the Gulf of Mexico constrained by altimetric Lagrangian coherent structures. *Geophys. Res. Lett.*, *40*, 6171–6175. doi: 10.1002/2013GL058624

Prants, S. V., Budyansky, M. V., & Uleysky, M. Y. (2018). How eddies gain, retain, and release water: A case study of a hokkaido anticyclone. *J. Geophys. Res.: Oceans*, *123*(3), 2081-2096.

Samelson, R. M. (2013). Lagrangian motion, coherent structures, and lines of persistent material strain. *Annu. Rev. Mar. Sci.*, *5*, 137–163. doi: 10.1146/annurev-marine-120710-100819

Schroeder, K., Chiggiato, J., Haza, A. C., Griffa, A., Özgökmen, T. M., Zanasca, P., ... Trees, C. (2012). Targeted lagrangian sampling of submesoscale dispersion at a coastal frontal zone. *Geophys. Res. Lett.*, *39*(11). doi: 10.1029/2012GL051879

Stepanov, D. V. (2017). Estimating the baroclinic Rossby radius of deformation in the Sea of Okhotsk. *Russian Meteorology and Hydrology*, *42*(9), 601–606. doi: 10.3103/S1068373917090072

Stepanov, D. V., Diansky, N. A., & Fomin, V. V. (2018). Eddy energy sources and mesoscale eddies in the Sea of Okhotsk. *Ocean Dynamics*, *68*, 825 – 845. doi: 10.1007/s10236-018-1167-3

Stepanov, D. V., Diansky, N. A., & Novotryasov, V. V. (2014). Numerical simulation of water circulation in the central part of the Sea of Japan and study of its long-term variability in 1958–2006. *Izvestiya, Atmospheric and Oceanic Physics*, *50*, 73–84. doi: 10.1134/S0001433813050149

Väli, G., Zhurbas, V. M., Laanemets, J., & Lips, U. (2018). Clustering of floating particles due to submesoscale dynamics: a simulation study for the gulf of finland, baltic sea. *Fundamentalnaya i Prikladnaya Gidrofizika*, *11*(2), 21-35. doi: 10.7868/S2073667318020028

Wang, Y., Olascoaga, M. J., & Beron-Vera, F. J. (2015). Coherent water transport across the south atlantic. *Geophys. Res. Lett.*, *42*(10), 4072-4079. doi: 10.1002/2015GL064089

Zhong, Y., & Bracco, A. (2013). Submesoscale impacts on horizontal and vertical transport in the gulf of mexico. *J. Geophys. Res.: Oceans*, *118*(10), 5651–5668. doi: 10.1002/jgrc.20402

Figure 1.

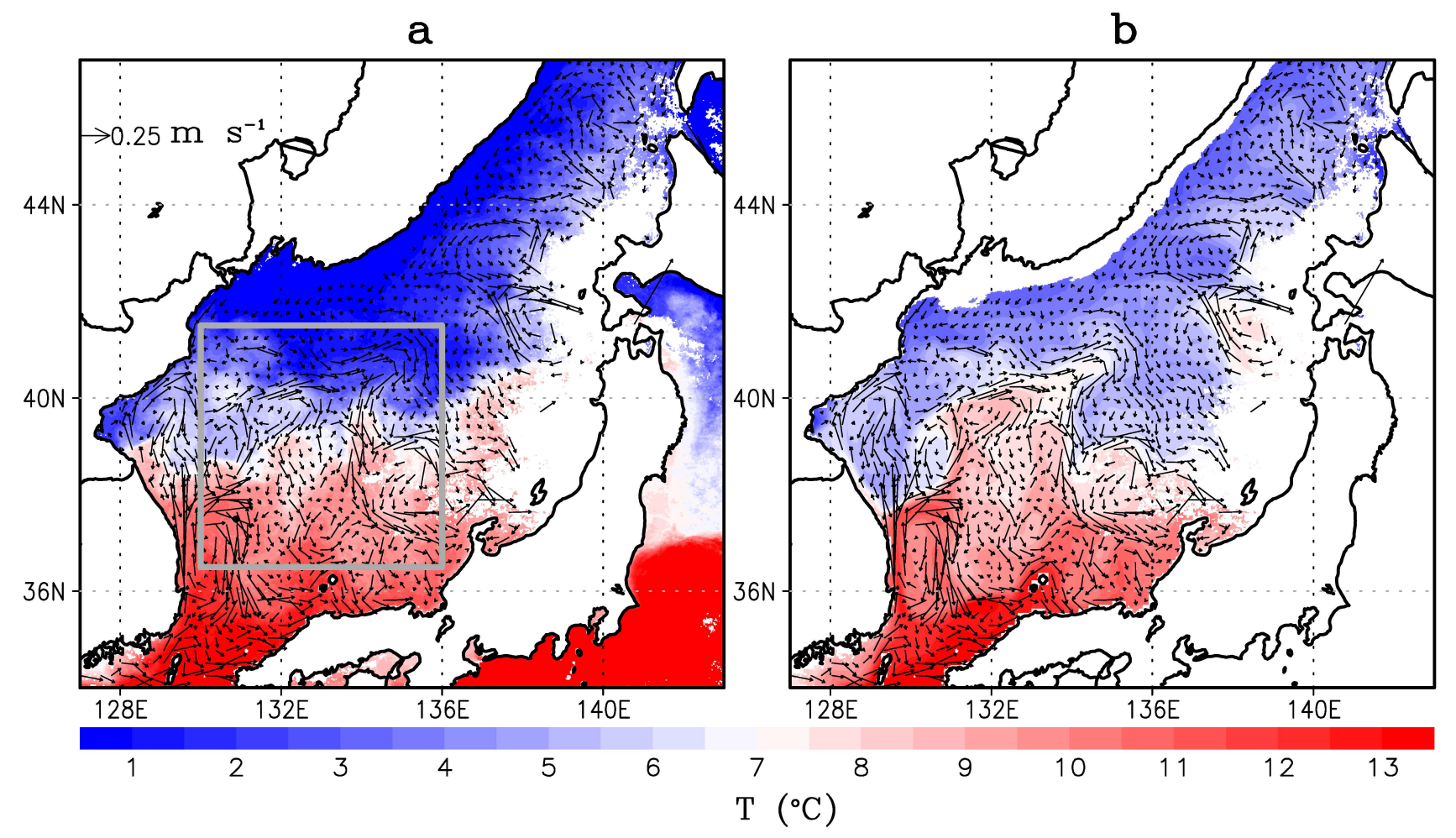
a
b
0.25 m s⁻¹
44N
40N
36N
128E
132E
136E
140E
1
2
3
4
5
6
7
8
9
10
11
12
13
T (°C)

Figure 2.

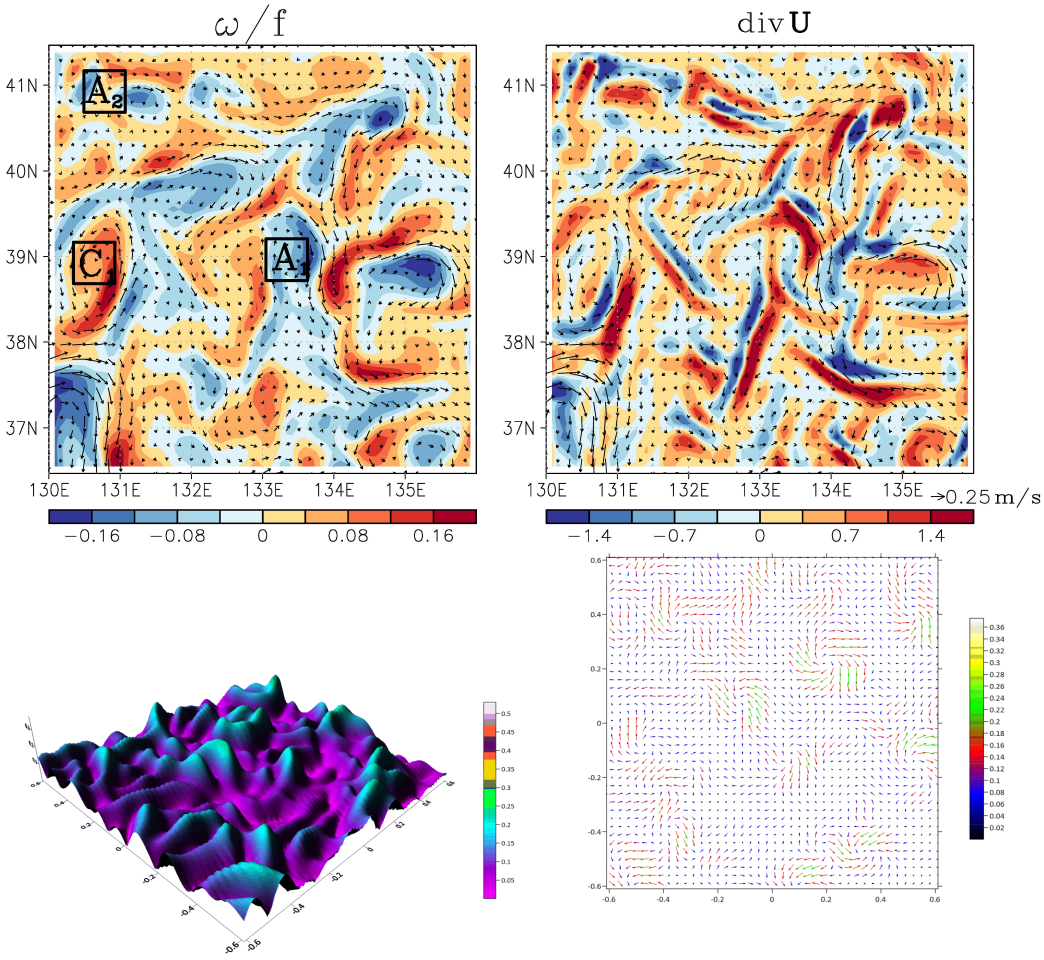
ω / f
div U
41N
40N
39N
38N
37N
130E
131E
132E
133E
134E
135E
A2
C
A1
−0.16
−0.08
0
0.08
0.16
−1.4
−0.7
0
0.7
1.4
→0.25 m/s

Figure 3.

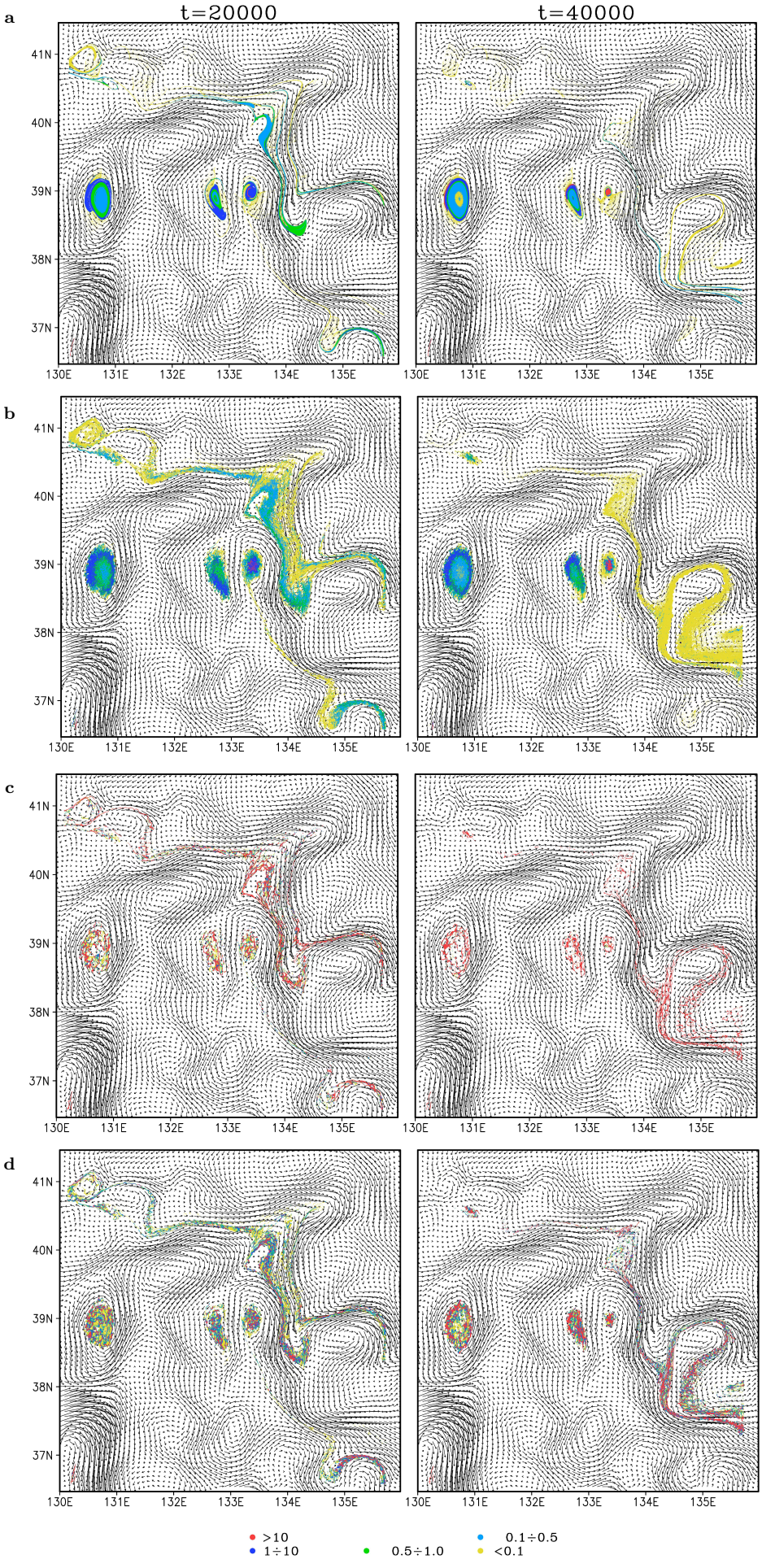
a
t=20000
t=40000
b
c
d
41N
40N
39N
38N
37N
130E
131E
132E
133E
134E
135E
>10
1÷10
0.5÷1.0
0.1÷0.5
<0.1

Figure 4.

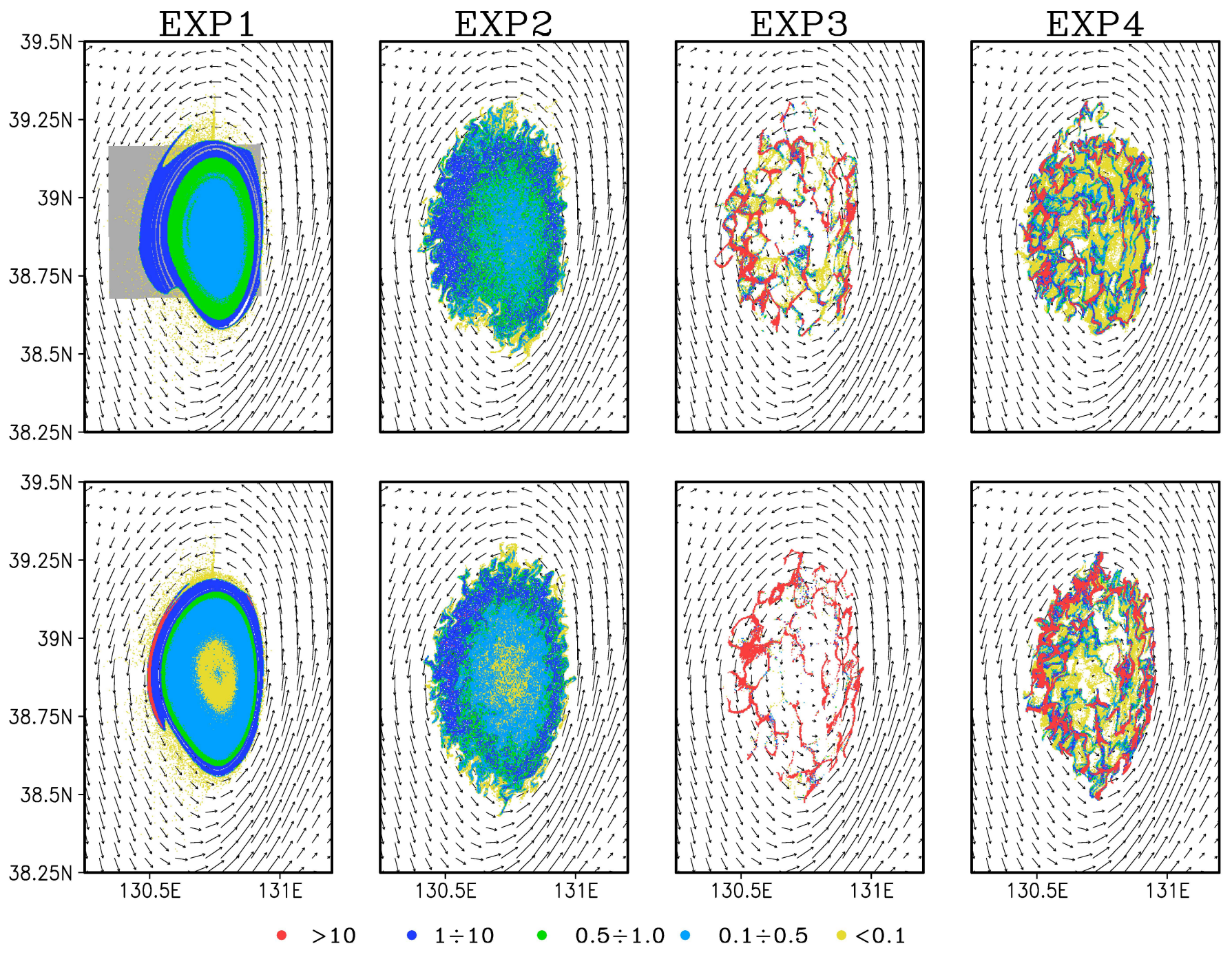
EXP1
EXP2
EXP3
EXP4
39.5N
39.25N
39N
38.75N
38.5N
38.25N
130.5E
131E
>10
1÷10
0.5÷1.0
0.1÷0.5
<0.1

Figure 5.

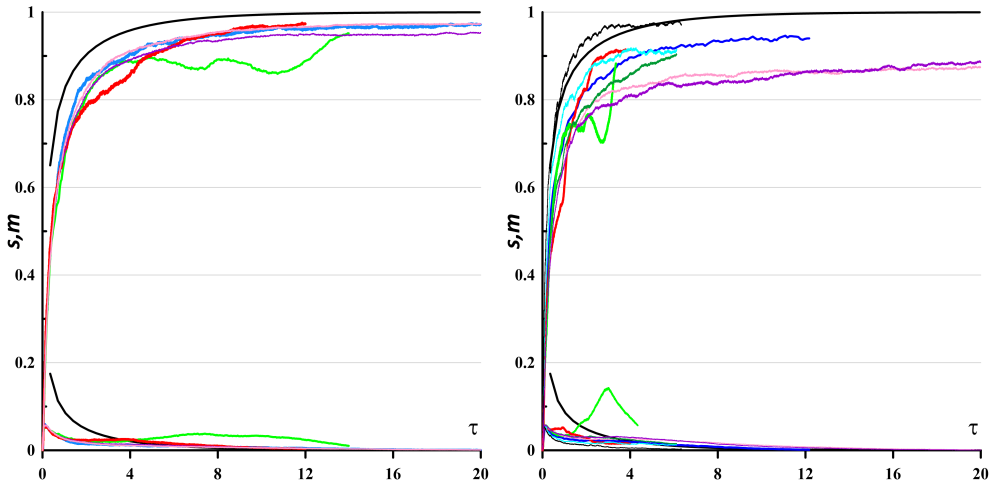
1
0.8
0.6
0.4
0.2
0
s,m
τ
0
4
8
12
16
20
1
0.8
0.6
0.4
0.2
0
s,m
τ
0
4
8
12
16
20

Figure 6.

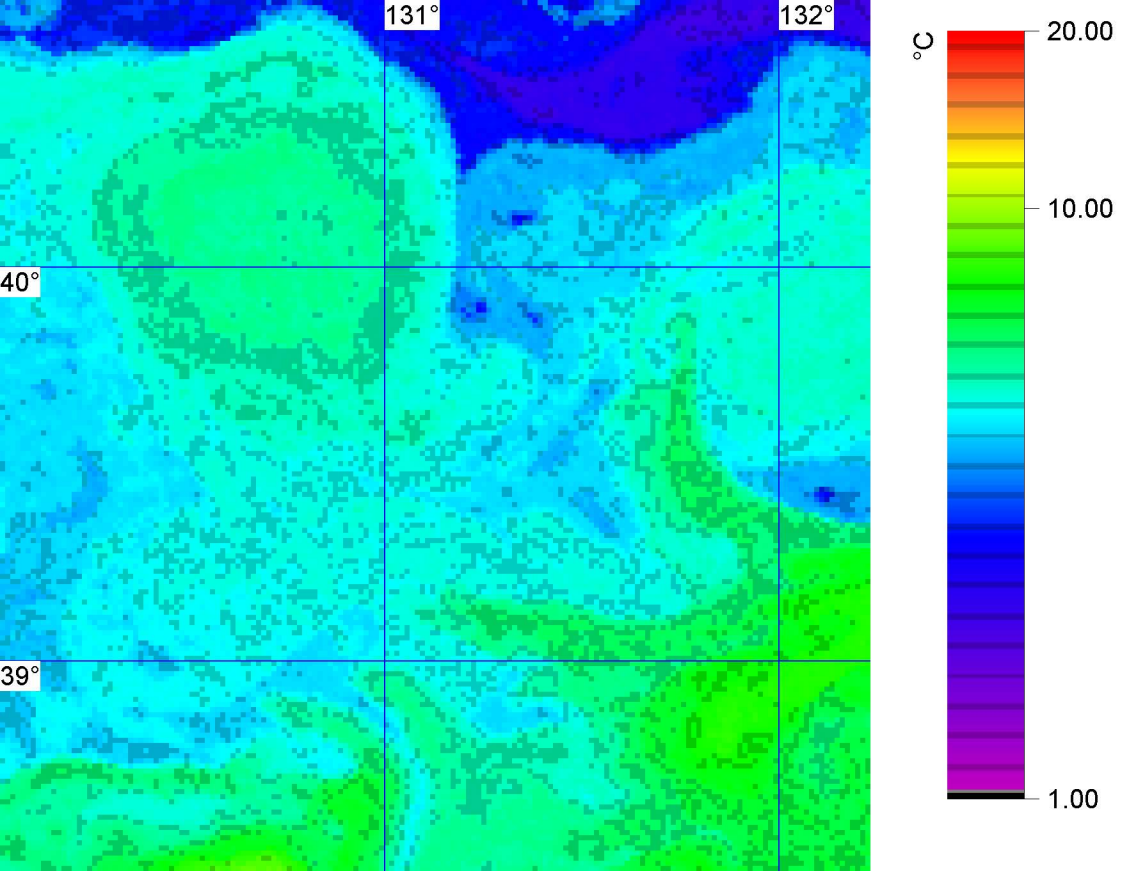
131°
132°
40°
39°
°C
20.00
10.00
1.00